Revisit of GeV Gamma-Ray Emission from Orion B with the Fermi Large Area Telescope

Wei Zeng[1], Xiao-Na Sun[1], Rui-Zhi Yang[2,3,4], Jia-Chun He[1], Zhao-Dong Shi[2,3,4] , Ting-Ting Ge[5], Yun-Feng Liang[1], and En-Wei Liang[1]

[1] Guangxi Key Laboratory for Relativistic Astrophysics, School of Physics Science and Technology, Guangxi University, Nanning 530004, China; xiaonasun@gxu.edu.cn
[2] Department of Astronomy, School of Physical Sciences, University of Science and Technology of China, Hefei 230026, China
[3] CAS Key Labrotory for Research in Galaxies and Cosmology, University of Science and Technology of China, Hefei 230026, China
[4] School of Astronomy and Space Science, University of Science and Technology of China, Hefei 230026, China
[5] School of Physics and Astronomy, Sun Yat-sen University, Zhuhai 519082, China

Abstract

We revisit the γ-ray emission above 300 MeV towards the massive star-forming region of Orion B by adopting 14 yr observations with the Fermi Large Area Telescope and utilizing the updated software tools. The extended γ-ray emission region around Orion B is resolved into two components (region I and region II). The γ-ray spectrum of region I agrees with the predicted γ-ray spectrum assuming the cosmic ray (CR) density is the same as that of Alpha Magnetic Spectrometer (AMS-02) measured locally. The γ-ray emissivity of region II appears to be deficit at low energy band ($E < 3$ GeV). Through modeling we find that CR densities exhibit a significant deficit below 20 GeV, which may be caused by a slow diffusion inside the dense region. This is probably caused by an increased magnetic field whose strength increases with the gas density.

Key words: (ISM:) cosmic rays – gamma-rays: ISM – (Galaxy:) open clusters and associations: individual (NGC 2023, NGC 2024,NGC 2068 and NGC 2071)

1. Introduction

Molecular Clouds (MCs) are significant targets for studying the origin of cosmic rays (CRs) (Gabici et al. 2007; Yang et al. 2014; Aharonian et al. 2020). Galactic CRs penetrate into the interior of MCs to produce γ-ray emissions (Aharonian 2001; Abdo et al. 2009b). Under this assumption, the flux of γ-ray depends on the mass of cloud (Aharonian et al. 2020). MCs within our galaxy are the birthplaces of many stars (Lada 1998).

Orion B is located at Orion star-forming region, with a distance of $\sim$400 pc. The mass of Orion B is $\sim$10$^5 M_\odot$ (Bally 2008). MC Orion B contains four stellar clusters, NGC 2023, NGC 2024, NGC 2068, and NGC 2071, with over a hundred stars including dozens of OB stars (Bally 2008). NGC 2023 includes 73 young stellar objects (YSOs) and has an early B star HD 37 903 (Mookerjea et al. 2009). The distance and mass of NGC 2023 are $\sim$420 pc (Kounkel et al. 2017) and $\sim$290$M_\odot$ (Lada 1992). NGC 2023 is a region of modest mass star formation triggered by the collision of two clouds (Yamada et al. 2021). NGC 2024 is the most active ionized hydrogen (H II) region in the southwest part of Orion B and is separated from nearby NGC 2023 by about 4 pc. The mass of NGC 2024 is $\sim$2 $\times$ 10$^3 M_\odot$ (Snell et al. 1984), including more than 300 stars and three OB stars with age less than 2 Myr (Bally 2008; Bik et al. 2003). Bik et al. (2003) pinpointed the source of ionization for NGC 2024 as IRS2b, which is the late-O to early-B star. NGC 2024 is a region of high-mass star formation triggered by the collision of two clouds, one situated at the forefront of the H II region and the other positioned internally or behind the H II region (Enokiya et al. 2021). Located at a distance of 388 pc in the northeastern part of the Orion B are two clusters, NGC 2068 and NGC 2071 (Kounkel et al. 2017). NGC 2068 includes 45 YSOs with the mass of 243$M_\odot$ and NGC 2071 includes 52 YSOs with the mass of 400$M_\odot$ (Spezzi et al. 2015). This star-forming region is triggered by the collision of cloud NGC 2068 and cloud NGC 2071 (Fujita et al. 2021).

The initial detection of γ-ray emissions from the Orion MC was made by the COS-B satellite (Caraveo et al. 1980; Bloemen et al. 1984). The Energetic γ-ray Experiment Telescope (EGRET) detected γ-ray emissions from Orion and found no evidence for variations of CRs density in Orion (Digel et al. 1995, 1999). Fermi Large Area Telescope (Fermi-LAT) further detected γ-ray emissions from Orion (Ackermann et al. 2012b), and found the $X_{\rm CO}$ of Orion B is smaller than the Galactic mean value (Ackermann et al. 2012b; Ripple et al. 2013). Yang et al. (2014) and Baghmanyan et al. (2020) analyzed the nearby GMCs including the Orion B with Fermi-LAT data. They found the CRs spectrum derived from the γ-ray spectrum agreed with the local measurements above 10 GeV. However, the CRs spectra below 10 GeV deviate from the spectra of the local

measurement, which is probably due to the propagation effects and local accelerators (Yang et al. 2014). The CRs deficit below 10 GeV is probably caused by the lack of penetration of CRs into denser regions (Yang et al. 2023).

No prominent non-thermal X-ray sources or radio supernova remnants have been detected around the Orion B cloud (Feigelson et al. 2002; Ackermann et al. 2012b). In the paper, we analyzed the GeV γ-ray emission associated with the embedded clusters in Orion B with available Fermi-LAT data. The structure of this paper is as follows. In Section 2, we analyze the distribution of gas around Orion B. In Section 3, we describe the data processing and its results. In Section 4, we calculate the CR spectrum and density. In Section 5, we summarize our results.

2. Gas Tracers

We studied three hydrogen phases toward the Orion B region, the molecular hydrogen (H_2), the neutral atomic hydrogen (H I), and the ionized hydrogen (H II). The 2.6 mm line of carbon monoxide (CO) is commonly used as a tracer with H_2. We used the CO composite survey with the CfA 1.2 m Millimeter-Wave Telescope (Dame et al. 2001). We assume that the column density of H_2 is proportional to the velocity-integrated brightness temperature of the CO 2.6 mm line, W_{CO}, such that $N(H_2) = X_{CO} \times W_{CO}$ (Lebrun et al. 1983). X_{CO} is the conversion factor for H_2/CO, which is adopted to be 2.0×10^{20} cm^{-2} K^{-1} km^{-1} s (Dame et al. 2001). We derive the column density of H_2 in Figure 1(a) using the velocity integration range of $v_{LSR} = [0, 15]$ km s^{-1} (Maddalena et al. 1986; Bally 2008).

The column density of H I is inferred from the H I 4π survey (HI4PI) data cube, a comprehensive 21 cm all-sky database of Galactic H I (HI4PI Collaboration et al. 2016). The equation can be expressed as

$$N_{H\,I}[\text{cm}^{-2}]$$
$$= -1.83 \times 10^{18} T_s \int dv \, \ln\left(1 - \frac{T_B}{T_s - T_{bg}}\right)[\text{K km s}^{-1}], \quad (1)$$

Here, T_B represents the brightness temperature, and $T_{bg} \approx 2.66$ K is the brightness temperature of the cosmic microwave background radiation at 21 cm. In this context when $T_B > T_s - 5$ K, we truncate T_B to $T_s - 5$ K; T_s is selected to be 150 K. The velocity range used here is the same as the derivation of H_2 column density. We derive the column density of H I in Figure 1(b).

NGC 2024 is a bright ionized hydrogen region. To obtain the H II column density distribution, we used the Planck free–free map (Planck Collaboration et al. 2016). We transformed the emission measurements to free–free intensity to calculate the H II column density with the conversion factor at 353 GHz from Table 1 of Finkbeiner (2003). We used Equation (5)

presented in reference Sodroski et al. (1997),

$$N_{H\,II} = 1.2 \times 10^{15} \text{ cm}^{-2}\left(\frac{T_e}{1\text{ K}}\right)^{0.35}\left(\frac{\nu}{1\text{ GHz}}\right)^{0.1}\left(\frac{n_e}{1\text{ cm}^{-3}}\right)^{-1}$$
$$\times \frac{I_\nu}{1\text{ Jy sr}^{-1}}, \quad (2)$$

where $\nu = 353$ GHz and $T_e = 8000$ K are the frequency and the electron temperature. The effective electron density, n_e, is directly proportional to the reciprocal of the column density of H II. We adopted a value of 2 cm^{-3} (Sodroski et al. 1997) for the effective density to derive the column density map of H II in Figure 1(c).

Neutral gas is not always traceable via CO and H Measurements due to various reasons (Grenier et al. 2005). In optically thick clouds, the infrared emission from cold interstellar dust serves as an alternative tracer, providing independent estimates of column density of gas. Then, we made a dust template from dust opacity map derived by the Planck collaboration (Planck Collaboration et al. 2011), it traces "dark gas" as well. We used the relationship between the column density of gas and dust opacity as described by Equation (4) of Planck Collaboration et al. (2011)

$$\tau_M(\lambda) = \left(\frac{\tau_D(\lambda)}{N_H}\right)^{\text{dust}}[N_{H\,I} + 2X_{co}W_{co}], \quad (3)$$

where $\tau_M(\lambda)$ represents the dust optical depth in relation to the wavelength λ, $(\tau_D/N_H)^{\text{dust}}$ denotes dust emissivity that can be found in Table 3 in Planck Collaboration et al. (2011). The replacement of the last into Equation (3) gives

$$N_H = N_{H\,I} + 2N_{H_2} = \tau_M(\lambda)\left[\left(\frac{\tau_D(\lambda)}{N_H}\right)^{\text{dust}}\right]^{-1}, \quad (4)$$

We used the dust emissivity at 353 GHz, $(\tau_D/N_H)^{\text{dust}} = (1.18 \pm 0.17) \times 10^{26}$ cm^{-2} to derive the column density of dust shown in Figure 1(d).

The estimation of mass of cloud for each individual pixel is derived using the expression

$$M_H = m_H N_H A_{\text{angular}} d^2, \quad (5)$$

where m_H, $N_H = N_{H\,II} + 2N_{H_2} + N_{H\,I}$, A_{angular}, and d are the mass of a single hydrogen atom, the total column density of hydrogen atom, the angular area, and the distance of clouds, respectively.

3. Fermi-LAT Data Analysis

We opted for the most recent Pass 8 data from Fermi-LAT toward Orion B, covering a period of more than 14 yr from 2008 August 4 (MET 239557417) to 2022 November 15 (MET 690167026). We chose the events with energy above 300 MeV. We employed the standard analysis software package version $v11r5p3$[6] provided by Fermi-LAT. A $14° \times 14°$ rectangular

---
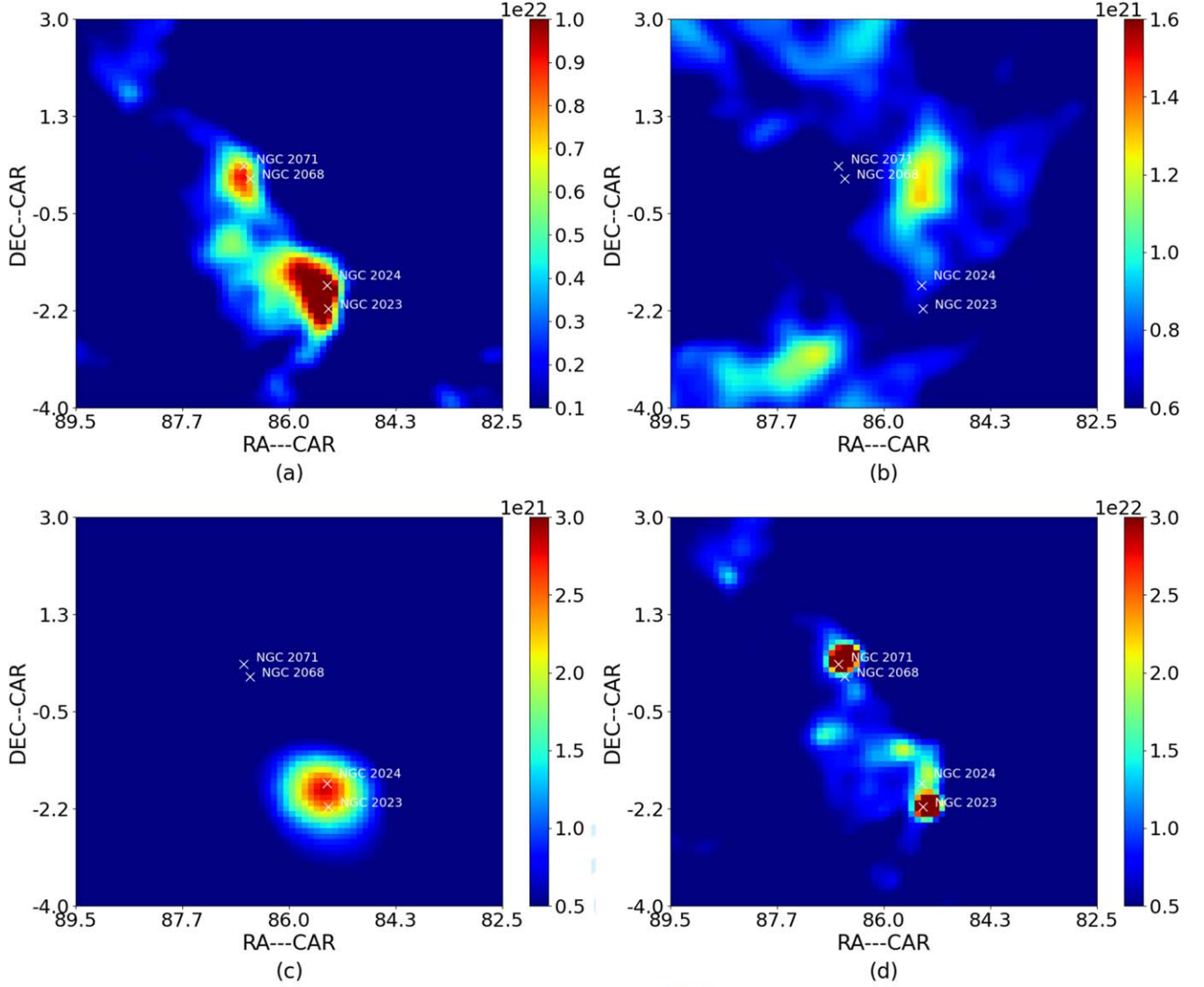
[6] https://fermi.gsfc.nasa.gov/ssc/data/analysis/software/

Figure 1. Gases distribution in the $7° \times 7°$ region around Orion B. (a) The map of H_2 column density derived from the CO data. (b) The map of H I column density. (c) The map of H II column density. (d) The map of dust column density. The white crosses indicate the star clusters.

region centered around the location of R.A. $= 86°.00$, decl. $= -0°.50°$ was designated as the region of interest (ROI). In order to minimize the impact of Earth albedo background, we employed a maximum zenith angle of $90°$ for the included events. We used the recommended expression (DATA_QUAL > 0)&&(LAT_CONFIG==1) to proceed with additional data refinement using the *gtmktime*. The spectral analysis was performed based on the current Fermitools obtained through conda distribution[7] with the instrument response functions (IRFs) of *P8R3_SOURCE_V3* version.

Photons converted both at the front and back sections of the detector were included in the selection. We employed the python module that applies a maximum likelihood optimization method for conducting the standard binned analysis.

As depicted in the left portion of Figure 2, we make the residual map above 300 MeV around the Orion B region subtracting all the catalog sources, the Fermi-LAT Galactic diffuse background model (gll_iem_v07.fits), and the extragalactic diffuse model *iso_P8R3_SOURCE_V3_v1.txt*.[8] We noted that there are two negative residuals (deficits) in Orion B,
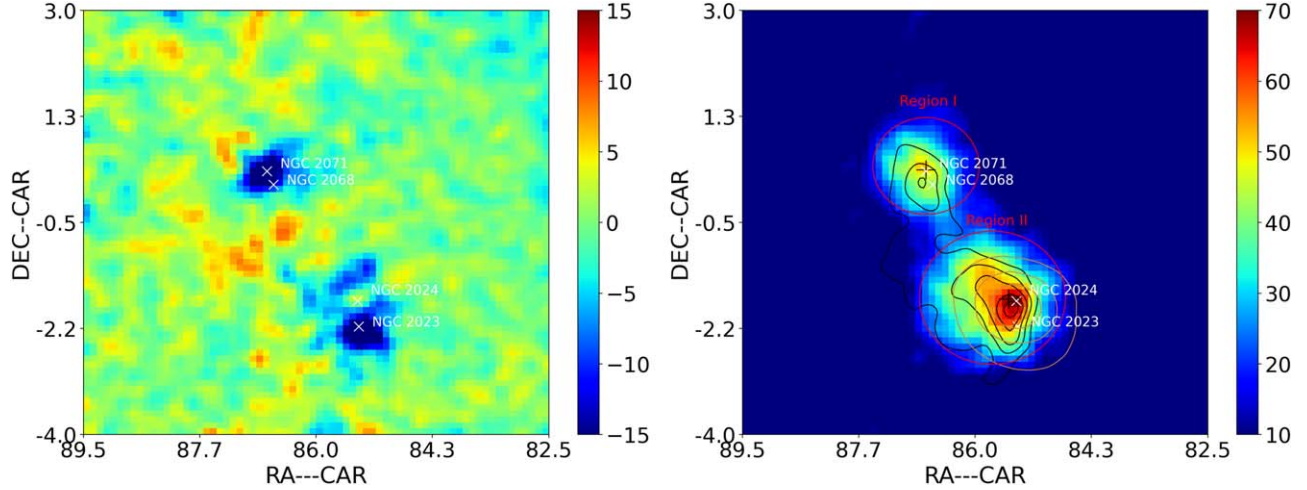
Figure 2. Residual map above 300 MeV in the $7° \times 7°$ region of Orion B with pixel size of $0°.1 \times 0°.1$. Left panel is derived from subtracting all cataloged sources and the Fermi-LAT Galactic diffuse background model (gll_iem_v07.fits). Right panel is derived from subtracting all cataloged sources and background components constructed in this work. The red circles represent regions I and II. The black pluses indicate the best-fit position of the assumed two point sources employed in the spatial analysis. The black and brown curves show the contours of column density of H_2 and H II.

one is located around the star cluster NGC 2071 and NGC 2068 and the other one is around the star cluster NGC 2024 and NGC 2023. The galactic interstellar emission model provided by Fermi collaboration[9] is not suitable for assessing the background in Orion B region, since the γ-ray emission around the molecular clouds is inherently part of the background.

To estimate the Galactic diffuse background components, we first estimated the inverse Compton (IC) scattering with GALPROP[10] (Vladimirov et al. 2011), which used the information regarding CRs electrons and interstellar radiation field (ISRF). We used the $^SY^Z6^R30^T150^C2$ template (Acero et al. 2016), which corresponds to the identical IC component in the Fermi-LAT standard Galactic interstellar emission model. This model is formulated based on the premise that CR sources are distributed proportionally to the known pulsar population (Yusifov & Küçük 2004) and CRs propagate within a Galactic halo characterized by a half-height of 6 kpc and a galactocentric radius of 30 kpc, adopting the diffusive reacceleration scenario. Then we constructed the template of the background clouds by a sum of the column density of H I and H_2 and H II ($N_{\mathrm{H\,I}} + 2N_{\mathrm{H_2}} + \mathrm{H\,II}$) in each pixel within the ROI. We cut out the Orion B cloud from the summation map and considered the rest as the gas background. We also included the point-like sources from the released Fermi-LAT 14 yr Source Catalog (4FGL-DR4, Ballet et al. 2023). The normalization of point-like sources, those with significance exceeding 5σ within $5°$ from the center of the ROI, was freely adjusted. Additionally, the extragalactic diffuse model iso_P8R3_SOURCE_V3_v1.txt was also incorporated.

Next we investigated the spatial morphology of γ-ray emissions around Orion B. The right panel of Figure 2 shows the residual map after subtracting all the catalog sources and the above background. We see that there are two positive residuals around the Orion B. We divided the excess of γ-ray emission into region I ($0°.8$) and region II ($1°.1$), using the size of the γ-ray emission profile marked by red circles. Region I encompasses NGC 2068 and NGC 2071, region II includes NGC 2023 and NGC 2024.

3.1. Two Point Sources Model

We first used two point-like sources to fit the γ-ray emissions of region I and II (model 1). The best-fit positions are (R. A. = $86°.79$, decl. = $0°.32$) for region I with 2σ error radius of $0°.02$ and (R.A. = $85°.55$, decl. = $-1°.81$) for region II with 2σ error radius of $0°.02$ obtained with the gtfindsrc tool. All the spectral types were assumed to be a log-parabola distribution. We conducted a binned likelihood analysis to obtain the likelihood value ($-\log(\mathcal{L})$) and the Akaike Information Criterion (AIC, Akaike 1974) value. The AIC is characterized as AIC $= -2\log(\mathcal{L}) + 2k$, with k representing the number of unfixed variables within the model. The resulting $-\log(\mathcal{L})$ and AIC were -309446 and -618822, respectively.

3.2. Two Uniform Disks Model

To investigate the extension of the GeV γ-ray emissions located in region I and region II, we employed a spatial template consisting of two uniform disks. For region I, we generated several uniform disks centered on the optimal fitting location for the region on the residual map, with radii ranging from $0°.3$ to $1°.0$ in steps of $0°.01$. We also created several

---

uniform disks for region II with radii ranging from $0°\!.5$ to $1°\!.2$ in steps of $0°\!.01$. Initially, we fixed the radius of region I to be $0°\!.65$, and then freed the radius of region II. We conducted a binned likelihood analysis on the events and derived the optimal radius of region II. Then we fixed the optimal radius of region II and freed the radius of region I. In the tests, we found that the uniform disks with the radii of $0°\!.74$ for the region I and $0°\!.91$ for the region II (model 2) best fitted the data. The obtained $-\log(\mathcal{L})$ and AIC were -311073 and -622072, respectively. We calculated the statistical significance corresponding to the source extension TS_{ext}. The TS_{ext} value is characterized as $TS_{ext} = 2\log(\mathcal{L}_{ext}/\mathcal{L}_{ps})$, where $\log(\mathcal{L}_{ext})$ and $\log(\mathcal{L}_{ps})$ represent the likelihood values of the extended two uniform disks model and two point-like sources model, respectively. The derived TS_{ext} is 3250, indicating a significance of extension of about 57σ compared to the two point sources model.

3.3. Two Gaussian Disks Model

We replaced the two uniform disks of model 2 with two Gaussian disks. We generated several Gaussian disks for region I with ranging radii from $0°\!.2$ to $0°\!.8$ in steps of $0°\!.01$, and likewise, for region II with ranging radii from $0°\!.4$ to $1°\!.0$ in steps of $0°\!.01$. We initially fixed the radius of region I to be $0°\!.45$, and freed the radius of region II. After performing the likelihood fitting, we found the best radius of region II. Then we fixed the best radius of region II and freed the radius of region I. We found that Gaussian disks with a radius of $0°\!.38$ for region I and a radius of $0°\!.47$ for region II (model 3) best fitted the data. The obtained $-\log(\mathcal{L})$ and AIC were -311208 and -622342, respectively.

3.4. Dust Model

The dust map includes not only H_2 and $H\,\textsc{i}$ but also incorporates contributions from dark gas. We also created the dust template (model 4) by dust opacity map (see Section 2). Here we should note that the dust opacity map does not contain any information about the distances and velocity, the derived column from dust opacity is integrated over the entire line of sight. After performing the binned likelihood analysis, the obtained $-\log(\mathcal{L})$ and AIC were -311117 and -622164, respectively.

3.5. Gas Model

As shown in the right panel of Figure 2, the black and brown curves represent the contours of column density distribution of H_2 and $H\,\textsc{ii}$, respectively. We can see the γ-ray emissions from both the region I and II have strong spatially correlation with the H_2 gas distribution. We produced the $H_2+H\,\textsc{i}$ template (model 5). By conducting a binned likelihood analysis, we obtained $-\log(\mathcal{L})$ and AIC for this model are -311407 and

Table 1
Results of Different Models

Model	$-\log(\mathcal{L})$	d.o.f.	ΔAIC
Model 1 (Two point sources)	-309446	35	$\cdots$
Model 2 (Two uniform disks)	-311073	37	-3250
Model 3 (Two Gaussian disks)	-311208	37	-3520
Model 4 (Dust template)	-311117	35	-3342
Model 5 ($H_2 + H\,\textsc{i}$ template)	-311407	35	-3922
Model 6 ($H_2 + H\,\textsc{i} + H\,\textsc{ii}$ template)	-311414	35	-3936

-622744, respectively. The derived TS_{ext} is 3922, indicating a significance of extension of about 63σ compared to the two point sources model. In addition, we observe that the γ-ray emission from region II is consistent with the $H\,\textsc{ii}$ gas distribution spatially, which supports the assumption that the γ-ray emission originates from the interaction between newly accelerated CRs with the surrounding gas. We produced the gas template (model 6), namely, the contribution of H_2, $H\,\textsc{i}$, and $H\,\textsc{ii}$. The obtained $-\log(\mathcal{L})$ and AIC for model 6 are -311414 and -622758, respectively. The derived TS_{ext} is 3936. The average column density of $H\,\textsc{ii}$ is significantly smaller than the column density of H_2 by an order of magnitude, thus the $H\,\textsc{ii}$ composition does not notably enhance the likelihood fit. We also calculated the ΔAIC to evaluate the quality of the fit of various models, among which model 1 and model 2–6. As shown in Table 1, the minimum ΔAIC for model 6 indicates that it is the best-fit model.

3.6. Spectral Analysis

We employed the optimal fit spatial model (model 6) and assumed a log-parabola spectral shape to derive the γ-ray spectra of both regions. We partitioned the energy range spanning from 300 MeV to 100 GeV into ten logarithmically bins. We estimated the 95% confidence level statistical uncertainties for the energy flux densities. For the first three energy bins, we considered the energy dispersion correction. We estimated the upper limits within 3σ for the energy bins with a significance lower than 2σ. To test the uncertainties of the Galactic diffuse emission background and the LAT effective area (A_{eff}), we artificially varied the spectral normalizations of the IC and $H_2 + H\,\textsc{i} + H\,\textsc{ii}$ background components by $\pm6\%$ from the optimal fit value for each energy bin, and considered the maximum flux deviation of the source as the systematic uncertainty Abdo et al. (2009a). We tested 16 sets of the IC templates to assess the uncertainties, using the related parameters from Ackermann et al. (2012a). The Lorimer distribution (Lorimer et al. 2006), Ysifov distribution (Yusifov & Küçük 2004), Supernova Remnants (SNR) distribution (Case & Bhattacharya 1998), and OB stars distribution (Bronfman et al. 2000) were separately selected for the CRs source distribution. The half height of the Galactic halo was
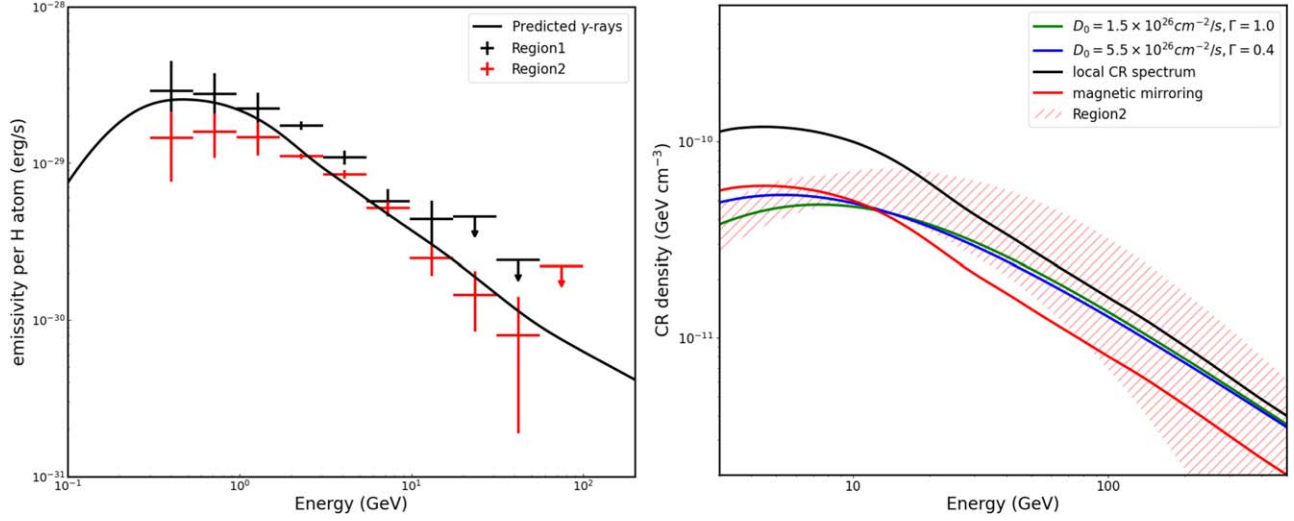
Figure 3. Left panel: SEDs derived from the model 6 (data points) for region I and region II. The black curve represents the predicted γ-ray emission. Right panel: the derived CR spectrum for region II. The red and black curves represent the predicted local CR density with and without the effect of the magnetic mirroring. The blue and green curves are CR spectra in the cloud center with the parameter of different values. The shaded areas denote 1σ for the fitted proton spectra.

assumed to be 4 kpc, 6 kpc, 8 kpc, and 10 kpc. Below 600 MeV, the results show a flux level variation of up to 12%, while at higher energies the changes become negligible.

The derived spectral energy distributions (SEDs) are depicted in the left panel of Figure 3. We normalized the γ-ray emission according to the emissivities per hydrogen atom, a measure that should scale proportionally with the CR density. The total masses of the gas within region I and region II are calculated to be $9.8 \times 10^3 \, M_\odot$ and $3.0 \times 10^4 \, M_\odot$. The black dashed line represents the predicted γ-ray emissivities assuming CR spectra are the same as those observed in the local interstellar medium as measured by AMS-02 (Aguilar et al. 2015). We found that the γ-ray emissivities derived from the gas template in region I are roughly agreed with the predicted γ-ray emissivities. This means that CRs can freely get through the clouds within region I, and observed γ-ray emissions around region I are from interaction between CR sea with the molecular content (diffuse background). The measured γ-ray emissivities from the gas template in region II show significant localized deficit at low energies ($E < 3 \, \text{GeV}$). The deficit of low-energy γ-rays might be explained by the proposition that the column density of gas in region II is overrated, which consequently reduces the γ-ray emissivities. However, an overestimation of the gas column density affects only the normalization of the spectrum and not the shape. The deficit in the γ-ray emissivity spectrum observed in region II suggest there are also deficit in the CR spectrum.

4. The CR Content of the Region II

In the following, we assumed that the γ-ray emissions around region II primarily originate from the proton-proton

inelastic interaction between CR and surrounding gases. We fitted the SEDs of the gas template in region II using Naima[11] (Zabalza 2015). To fit the observation of γ-ray emissions, we used a broken power-law proton spectrum,

$$N(E) = \begin{cases} A(E/E_0)^{-\alpha_1}, & E < E_\text{b} \\ A(E_\text{b}/E_0)^{(\alpha_2 - \alpha_1)}(E/E_0)^{-\alpha_2}, & E > E_\text{b} \end{cases}, \quad (6)$$

to constrain data points, we fixed E_b to be 30 GeV. The derived parameters are $\alpha_1 = 2.0 \pm 0.3$, $\alpha_2 = 3.7 \pm 0.5$.

We obtained the CR spectrum base on the best-fit γ-ray spectrum. The CR energy density can be described as,

$$\omega_\text{p} = \frac{L_\gamma}{k N_\text{p} v_\text{CR} \sigma_\text{pp}}, \quad (7)$$

where L_γ and N_p are the γ-ray luminosity and the number of protons, respectively. We approximate the velocity of CR protons to be 0.9 times the speed of light, v_CR, using 10 GeV photon energy. We employed the cross section of interaction $\sigma_\text{pp}(E_\text{p})$ from (Kafexhiu et al. 2014). The parameter $k \sim 0.17$ represents the fraction of energy that is transferred from the proton to the pion during their interaction (Kelner et al. 2006). The derived CR spectrum from the region II exhibits prominent localized deficit at lower energies ($E < 20 \, \text{GeV}$) depicted in the right portion of Figure 3.

Taking into account four OB stars exist in the clusters NGC 2023 and NGC 2024, if the kinematic luminosity provided by the stellar wind of one massive star is $1.0 \times 10^{35} \, \text{erg s}^{-1}$ (Fukushima et al. 2023), the estimated total kinematic luminosity is about $4 \times 10^{35} \, \text{erg s}^{-1}$. In addition, there are

---

[11] https://naima.readthedocs.io/en/latest/index.html

about fifteen OB stars within region II using the webpage SIMBAD,[12] and the estimated total kinematic luminosity is about $1.5 \times 10^{36} \, \mathrm{erg \, s^{-1}}$. Such powerful stellar winds may effectively obstruct the penetration of CRs from the interstellar medium (ISM) into the region II, leading to the CR deficit. The effectiveness of CR modulation depends on the overall strength of the stellar winds driven by young stars. The number of OB stars in Region I and Region II of Orion B is basically same, which would not result in major differences in the CR deficit. While, with the current data, we found significant difference in the γ-ray spectra for different regions, although given the current statistics, we cannot rule out such a scenario yet. Additionally, protostellar outflows are not volume-filling, and their role in CR shielding should be limited (Yang et al. 2023). In view of the above arguments, we would not discuss this scenario in detail.

Magnetic mirroring phenomena can similarly hinder CRs from penetrating the MC. We used the method in the paper (Owen et al. 2021) to estimate such effects. The $\eta(\chi) = (\chi - \sqrt{\chi^2 - \chi})$ is the coefficient of CR flux within the cloud, where χ is the ratio of the magnetic field strength of cloud compared to the mean ISM value, $\eta(\chi)$ saturated to 0.5 quickly when $\chi > 2$. We plotted the predicted CR density taking into account the magnetic mirroring illustrated in the right portion of Figure 3. The predicted CR density inside the cloud taking into account the magnetic mirroring is reduced by approximately 50% compared with the predicted CR density. Thus, the magnetic mirroring alone is insufficient to explain the spectral shape of region II.

The slower diffusive transport within the dense molecular may lead to the CR deficits in lower energies (Gabici et al. 2007; Yang et al. 2023). To verify whether this hypothesis is consistent with our observations, we describe the propagation of CR using Equation (6) of Gabici et al. (2007),

$$\frac{dN}{dt} = \frac{1}{R^2} \frac{\partial}{\partial R} \left(D(R, E) R^2 \frac{\partial N}{\partial R} \right) + \frac{\partial}{\partial E} (\dot{E} N), \qquad (8)$$

where N is particle distribution function of CRs, R is the distance to the center of the cloud, D is the diffusion coefficient, and $\dot{E}$ is the energy loss rate of CR protons. We assume a flat density profile and the locally measured CR spectrum as boundary conditions. The normalization is adjusted so that a total of $1500 M_\odot$ is contained in a region of ~ 1 pc. We adopted the general form of the diffusion coefficient as $D(E) = D_0 (\frac{E}{1 \, \mathrm{GeV}})^\Gamma$, where D_0 represents the reference value of the diffusion coefficient at an energy level of 1 GeV, and Γ serves as the exponent parameter that characterizes the energy-dependent coefficient. Γ is highly uncertain depending on the power spectrum of the magnetic field turbulence. We adjusted it within the physically realistic ranges from 0 (energy-independent diffusion) to 1 (Bohm-type diffusion) to
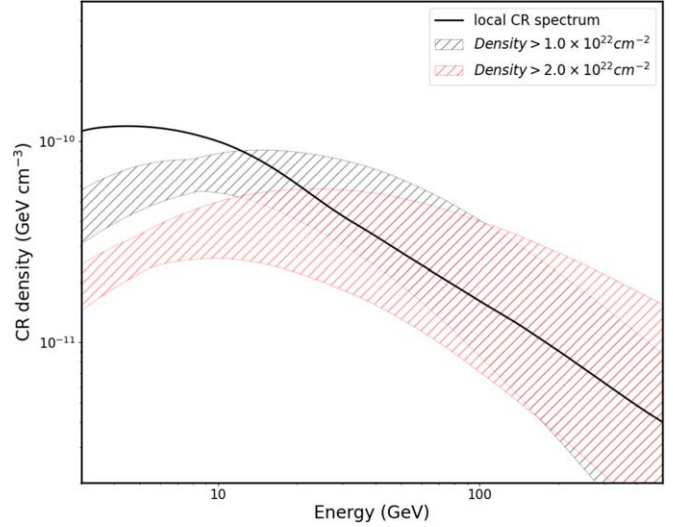
Figure 4. The derived CR spectra for dense cores. The black curves represent the local CR spectrum (Aguilar et al. 2015). The shaded regions of black and red represent the dense core are separated above the column density of $1.0 \times 10^{22} \, \mathrm{cm^{-2}}$ and $2.0 \times 10^{22} \, \mathrm{cm^{-2}}$, respectively. The shaded areas denote 1σ for the fitted proton spectra.

constrain the value of D_0. We found that D_0 cannot be outside the interval 1.5×10^{26}–$5.5 \times 10^{26} \, \mathrm{cm^2 \, s^{-1}}$. We found that the D_0 around 1 GeV is smaller than that in the ISM by two orders of magnitude. Two schematic fittings with different Γ are illustrated in the right portion of Figure 3. We find that our observation need a slower diffusion characterized by a smaller diffusion coefficient.

The slower diffusion in region II probably caused by the increased magnetic field, which increases with the gas density (Crutcher 2012; Yang et al. 2023). To check the impact of the average gas density on the CR deficit, we separated the $H_2 + H \, \mathrm{I} + H \, \mathrm{II}$ template into dense cores, of which the gas column density are above $1.0 \times 10^{22} \, \mathrm{cm^{-2}}$ and $2.0 \times 10^{22} \, \mathrm{cm^{-2}}$, respectively. The derived CR spectra of dense cores are illustrated in Figure 4. We found the CR spectra for the dense cores at higher energies are basically consistent with the local CR spectrum. The observed CR spectra for dense cores are significantly lower compared to the local CR spectrum below a few GeV and the suppression is more pronounced when the column density cut is $2.0 \times 10^{22} \, \mathrm{cm^{-2}}$. The higher average density indeed induce stronger CR shielding in the lower energy band.

5. Summary

The Fermi-LAT data with more time exposure enables us to further analyze the γ-ray emissions toward the Orion B, which is a star-forming region with four clusters. We find the extended γ-ray emissions in projection on the sky in the vicinity of this star-forming region can be separated into two

regions. Both regions show spatial correlation with the dense gases. This implies that the high energy γ-ray emissions around the GMC Orion B may produced by CR interactions with the dense ambient gas. The γ-ray emissions of both regions are well modeled by the $H_2 + H\,\text{I} + H\,\text{II}$ template. However, we find that the spectra of the two regions have significantly different characteristics.

The γ-ray spectrum derived in region I, taking into account the uncertainties, agrees with the predicted γ-ray spectrum illustrated in the left panel of Figure 3. This implies that the γ-ray emissions of region I mainly produce by the interactions of CR sea with the molecular content, and CRs can penetrate freely through clouds within region I. The measured γ-ray emissions from the gas template in region II show significant localized deficit at low energies ($E < 3\,\text{GeV}$). The deficit in γ-ray spectrum at low energies can potentially be attributed to the deficit of CRs below approximately 20 GeV. The strong stellar winds (about $0.4 \sim 1.4 \times 10^{36}\,\text{erg s}^{-1}$) of the young stars in region II probably prevent the low-energy CRs to enter into dense regions (Huang et al. 2021; Yang et al. 2023), which leads to the deficit of CRs. In addition, the slower diffusion described by a smaller diffusion coefficient (1.5×10^{26}–$5.5 \times 10^{26}\,\text{cm}^2\,\text{s}^{-1}$) can sufficiently describe deficit of CRs. Due to the higher gas density, the magnetic field in region II may be stronger (Crutcher 2012). The strong magnetic field will lead to slower diffusion (Yang et al. 2023). The CR deficit in region II become more significant with the increase of average density of the core region illustrated in Figure 4. Therefore, the deficit of γ-ray spectrum may be caused by the propagation effects that the lack of penetration of CRs at energies in the sub-GeV to GeV range into denser regions. Spectral characteristics of CRs linked to such propagation mechanisms have been detected in other denser regions of Taurus and Perseus clouds (Yang et al. 2023). Further studies with multi-wavelength spatial and spectral information are required to understand the injection and propagation of CRs in the vicinity of Orion B.

ORCID iDs

Zhao-Dong Shi ● https://orcid.org/0009-0009-1182-341X

References

Abdo, A. A., Ackermann, M., Ajello, M., et al. 2009a, ApJL, 706, L1
Abdo, A. A., Ackermann, M., Ajello, M., et al. 2009b, ApJ, 703, 1249
Acero, F., Ackermann, M., Ajello, M., et al. 2016, ApJS, 223, 26
Ackermann, M., Ajello, M., Allafort, A., et al. 2012b, ApJ, 756, 4
Ackermann, M., Ajello, M., Atwood, W. B., et al. 2012a, ApJ, 750, 3
Aguilar, M., Aisa, D., Alpat, B., et al. 2015, PhRvL, 114, 171103
Aharonian, F. A. 2001, SSRv, 99, 187
Aharonian, F., Peron, G., Yang, R., Casanova, S., & Zanin, R. 2020, PhRvD, 101, 083018
Akaike, H. 1974, ITAC, 19, 716
Baghmanyan, V., Peron, G., Casanova, S., Aharonian, F., & Zanin, R. 2020, ApJL, 901, L4
Ballet, J., Bruel, P., Burnett, T. H., Lott, B. & The Fermi-LAT collaboration 2023, arXiv:2307.12546
Bally, J. 2008, in Handbook of Star Forming Regions, ed. B. Reipurth, Vol. 4 (San Francisco, CA: APS), 459
Bik, A., Lenorzer, A., Kaper, L., et al. 2003, A&A, 404, 249
Bloemen, J. B. G. M., Caraveo, P. A., Hermsen, W., et al. 1984, A&A, 139, 37
Bronfman, L., Casassus, S., May, J., & Nyman, L. Å. 2000, A&A, 358, 521
Caraveo, P. A., Bennett, K., Bignami, G. F., et al. 1980, A&A, 91, L3
Case, G. L., & Bhattacharya, D. 1998, ApJ, 504, 761
Crutcher, R. M. 2012, ARA&A, 50, 29
Dame, T. M., Hartmann, D., & Thaddeus, P. 2001, ApJ, 547, 792
Digel, S. W., Aprile, E., Hunter, S. D., Mukherjee, R., & Xu, F. 1999, ApJ, 520, 196
Digel, S. W., Hunter, S. D., & Mukherjee, R. 1995, ApJ, 441, 270
Enokiya, R., Ohama, A., Yamada, R., et al. 2021, PASJ, 73, S256
Feigelson, E. D., Broos, P., Gaffney, J. A. I., et al. 2002, ApJ, 574, 258
Finkbeiner, D. P. 2003, ApJS, 146, 407
Fujita, S., Tsutsumi, D., Ohama, A., et al. 2021, PASJ, 73, S273
Fukushima, A., Ezoe, Y., & Odaka, H. 2023, PASJ, 75, 187
Gabici, S., Aharonian, F. A., & Blasi, P. 2007, Ap&SS, 309, 365
Grenier, I. A., Casandjian, J.-M., & Terrier, R. 2005, Sci, 307, 1292
HI4PI Collaboration, Ben Bekhti, N., Flöer, L., et al. 2016, A&A, 594, A116
Huang, X., Yuan, Q., & Fan, Y.-Z. 2021, NatCo, 12, 6169
Kafexhiu, E., Aharonian, F., Taylor, A. M., & Vila, G. S. 2014, PhRvD, 90, 123014
Kelner, S. R., Aharonian, F. A., & Bugayov, V. V. 2006, PhRvD, 74, 034018
Kounkel, M., Hartmann, L., Loinard, L., et al. 2017, ApJ, 834, 142
Lada, E. A. 1992, ApJL, 393, L25
Lada, E. A. 1998, in ASP Conf. Ser. 148, Origins, ed. C. E. Woodward et al. (San Francisco, CA: ASP), 198
Lebrun, F., Bennett, K., Bignami, G. F., et al. 1983, ApJ, 274, 231
Lorimer, D. R., Faulkner, A. J., Lyne, A. G., et al. 2006, MNRAS, 372, 777
Maddalena, R. J., Morris, M., Moskowitz, J., & Thaddeus, P. 1986, ApJ, 303, 375
Mookerjea, B., Sandell, G., Jarrett, T. H., & McMullin, J. P. 2009, A&A, 507, 1485
Owen, E. R., On, A. Y. L., Lai, S.-P., & Wu, K. 2021, ApJ, 913, 52
Planck Collaboration, Ade, P. A. R., Aghanim, N., et al. 2011, A&A, 536, A19
Planck Collaboration, Adam, R., Ade, P. A. R., et al. 2016, A&A, 594, A10
Ripple, F., Heyer, M. H., Gutermuth, R., Snell, R. L., & Brunt, C. M. 2013, MNRAS, 431, 1296
Snell, R. L., Mundy, L. G., Goldsmith, P. F., Evans, N. J. I., & Erickson, N. R. 1984, ApJ, 276, 625
Sodroski, T. J., Odegard, N., Arendt, R. G., et al. 1997, ApJ, 480, 173
Spezzi, L., Petr-Gotzens, M. G., Alcalá, J. M., et al. 2015, A&A, 581, A140
Vladimirov, A. E., Digel, S. W., Jóhannesson, G., et al. 2011, CoPhC, 182, 1156
Yamada, R. I., Enokiya, R., Sano, H., et al. 2021, PASJ, 73, 880
Yang, R.-z., de Oña Wilhelmi, E., & Aharonian, F. 2014, A&A, 566, A142
Yang, R.-z., Li, G.-X., Wilhelmi, E. d., et al. 2023, NatAs, 7, 351
Yusifov, I., & Küçük, I. 2004, A&A, 422, 545
Zabalza, V. 2015, in Proc. 34th Int. Cosmic Ray Conf. (ICRC2015), 34 (The Netherlands: ICRC), 922